

PHOTON DOMINATED REGIONS IN LOW UV FIELDS: A STUDY OF THE PERIPHERAL REGION OF L1204/S140

WENBIN LI

Department of Astronomy, The University of Texas at Austin
Austin, TX 78712

and

Enterprise Services, Sun Microsystems of Canada, Inc.
15 Allstate Parkway, Suite #300,
Markham, ONT L3R 5B4, Canada
wenbin.li@canada.sun.com

NEAL J. EVANS II

Department of Astronomy, The University of Texas at Austin
Austin, TX 78712, and Sterrewacht Leiden, P.O.Box 9513, 2300 RA Leiden, the Netherlands
nje@astro.as.utexas.edu

DANIEL T. JAFFE

Department of Astronomy, The University of Texas at Austin
Austin, TX 78712
dtj@astro.as.utexas.edu

EWINE F. VAN DISHOECK¹

Sterrewacht Leiden, P.O.Box 9513, 2300 RA Leiden, the Netherlands
ewine@strw.LeidenUniv.nl

WING-FAI THI

Sterrewacht Leiden, P.O.Box 9513, 2300 RA Leiden, the Netherlands
thi@strw.LeidenUniv.nl

L^AT_EXed at 1232 min., December 3, 2018

ABSTRACT

We have carried out an in-depth study of the peripheral region of the molecular cloud L1204/S140, where the far-ultraviolet radiation and the density are relatively low. Our observations test theories of photon-dominated regions (PDRs) in a regime that has been little explored. Knowledge of such regions will also help to test theories of photoionization-regulated star formation. [C II] 158 μm and [O I] 63 μm lines are detected by ISO at all 16 positions along a 1-dimensional cut in right ascension. Emission from H₂ rotational transitions $J = 2 \rightarrow 0$ and $J = 3 \rightarrow 1$, at 28 and 17 μm , was also detected at several positions. The [C II], [O I], and H₂ intensities along the cut show much less spatial variation than do the rotational lines of ¹²CO and other CO isotopes. The average [C II] and [O I] intensities and their ratio are consistent with models of PDRs with low far-ultraviolet radiation (G_0) and density. The best-fitting model has $G_0 \sim 15$ and density, $n \sim 10^3 \text{ cm}^{-3}$. Standard PDR models underpredict the intensity in the H₂ rotational lines by up to an order of magnitude. This problem has also been seen in bright PDRs and attributed to factors, such as geometry and gas-grain drift, that should be much less important in the regime studied here. The fact that we see the same problem in our data suggests that more fundamental solutions, such as higher H₂ formation rates, are needed. Also, in this regime of low density and small line width, the [O I] line is sensitive to the radiative transfer and geometry. Using the ionization structure of the models, a quantitative analysis of timescales for ambipolar diffusion in the peripheral regions of the S140 cloud is consistent with a theory of photoionization-regulated star formation. Observations of [C II] in other galaxies differ both from those of high G_0 PDRs in our galaxy and from the low G_0 regions we have studied. The extragalactic results are not easily reproduced with mixtures of high and low G_0 regions.

Subject headings: Infrared: ISM: lines and bands — Infrared: ISM: continuum — ISM: clouds (L1204/S140) — ISM: atoms — ISM: molecules

1. INTRODUCTION

Photon-dominated regions (or photodissociation regions, PDRs) are regions of the neutral interstellar medium (ISM) where far-ultraviolet (FUV) ($6 \text{ eV} < h\nu < 13.6 \text{ eV}$) photons control the heating and chemical processes. They are the interface between H II regions and cold molecular cores. The physical and chemical structure of PDRs depends critically on the FUV intensity and the gas density. In the peripheral regions of the molecular cloud

L1204/S140, the FUV intensity and the gas density are low, allowing tests of the models in an important regime. We are motivated by two primary goals: understanding PDRs in a regime of parameter space that has not been extensively studied; and understanding the role of the regions with relatively low FUV and density in global star formation, both in our own Galaxy and in other galaxies.

A great deal of observational and theoretical effort has been devoted to understanding PDRs. Comprehensive models of PDRs have been constructed by several groups

¹ The Beatrice M. Tinsley Centennial Visiting Professor, the University of Texas at Austin.

(e.g., Black & Dalgarno 1977, van Dishoeck & Black 1986, 1988, Tielens & Hollenbach 1985a, Sternberg & Dalgarno 1989, le Bourlot et al. 1993, Kaufman et al. 1999) by solving the full chemistry and heating-cooling balance in a self-consistent way. In PDRs with $n \leq 10^5 \text{ cm}^{-3}$, the most important heating process for gas is photoelectric heating—electrons ejected from dust particles by FUV photons heat the gas through collisions. For dust, direct absorption of FUV photons is the primary heating mechanism. Far-infrared continuum emission is the major cooling process for dust, and the far-infrared lines of $[\text{C II}] \ ^2\text{P}_{3/2} \rightarrow ^2\text{P}_{1/2}$ at $157.7409 \ \mu\text{m}$ (hereafter $[\text{C II}]$) and $[\text{O I}] \ ^3\text{P}_1 \rightarrow ^3\text{P}_2$ at $63.183705 \ \mu\text{m}$ (hereafter $[\text{O I}]$) are the most important for gas. Therefore, the $[\text{C II}]$ and $[\text{O I}]$ lines, along with H_2 rotational emission, are the most important tracers of PDRs.

Most previous work has focused on bright PDRs very close to hot OB stars, e.g., the Orion bar (Tielens & Hollenbach 1985b; Jansen et al. 1995; Hogerheijde et al. 1995; Tauber et al. 1994), the NGC 2023 PDR (Steiman-Cameron et al. 1997, Draine & Bertoldi 1996), and the S140 PDR (Emery et al. 1996; Timmermann et al. 1996; Spaans & van Dishoeck 1997). Other recent studies include those by Liseau et al. (1999), and the field has been reviewed by Draine & Bertoldi (1999) and by Hollenbach & Tielens (1999). These regions have a far-ultraviolet intensity of $G_0 > 10^3$ and a density higher than 10^4 cm^{-3} , where G_0 is the enhancement factor relative to the standard interstellar radiation field as given by Habing (1968).

There has been very little exploration of the physics of PDRs with modest far-ultraviolet fields and densities, conditions likely to prevail over most of the surface of molecular clouds in our Galaxy. Federman et al. (1995) and van Dishoeck & Black (1988) have studied PDRs in diffuse clouds ($A_V \sim 1 \text{ mag}$) and translucent clouds ($n < 1000 \text{ cm}^{-3}$, $G_0 < 17$ and $A_V < 5 \text{ mag}$). Regions with high densities and moderate UV fields ($n < 5 \times 10^4 \text{ cm}^{-3}$, $G_0 = 900$) have also been studied in some detail (Jansen et al. 1995), and Kemper et al. (1999) have used submillimeter and far-infrared observations to probe a reflection nebula with $n \sim 5000 \text{ cm}^{-3}$ and $G_0 \sim 200$. In this paper, we explore the critical intermediate regime where $n \equiv n(\text{H}) + 2n(\text{H}_2) \sim 500 - 5000 \text{ cm}^{-3}$ and $G_0 \sim 10 - 60$. The Infrared Space Observatory (ISO²) provided a unique opportunity to observe low-brightness extended $[\text{C II}]$, $[\text{O I}]$, and H_2 . We used this capability to study the intermediate regime.

It is also important to understand the role of regions with modest extinction and column density in star formation. Regions like those we are studying include most of the mass in the interstellar medium (Hollenbach & Tielens 1995), but their role in star formation is poorly known. Based on the Jeans criterion, most molecular clouds in the Galaxy are not sufficiently supported by thermal energy and therefore should collapse under gravity to form stars. Such widespread collapse, however, would lead to a Galactic star formation rate hundreds of times higher than what has been observed (Zuckerman & Palmer 1974, Evans 1991). The observed low star formation rate seems to indicate that most parts of most molecular clouds are “sterile” (Evans 1999). Magnetic fields and turbulence are

generally considered to play an important role in supporting molecular clouds and preventing or slowing collapse. However, there is no widely accepted theory on the mechanism of magnetic and turbulent support of molecular clouds. Recently, Elmegreen (2000) has argued that star formation does in fact happen within a few cloud crossing times, removing the need for cloud support. Pringle, Allen, & Lubow (2001) have pointed out that such a picture strains methods of cloud formation, and they conclude that visible clouds would have to form out of “dark” molecular matter. These scenarios beg the question: what prevents star formation in the great majority ($\sim 98\%$) of molecular gas?

McKee (1989; Bertoldi & McKee 1996, 1997) proposed a mechanism of photoionization-regulated star formation to explain the low star formation rate in the Galaxy by combining two ideas: first, that magnetic fields support molecular clouds; and second, that PDRs occupy a large fraction of molecular gas. The timescale for ambipolar diffusion is proportional to the ionization fraction ($x(e) = n(e)/n$) and the FUV photons and cosmic rays are the sources of ionization. Most molecular gas is sterile because it resides in a PDR, where the ionization is high enough to slow ambipolar diffusion. Only highly shielded regions are likely to form stars. In addition, newly formed stars inject energy into the clouds, replenishing turbulence and slowing star formation in the rest of the cloud. In this picture, molecular clouds reach dynamic equilibrium when $A_V \sim 8 \text{ mag}$. By focusing on a peripheral region, we test the conditions in these regions, which should not be forming stars according to the theory.

We have chosen a 1-D positional cut—we call it the S140 cut—in the peripheral region of the molecular cloud L1204 (Figure 1) for our PDR and chemistry study. S140, at distance of $\sim 910 \text{ pc}$ (Crampton & Fisher 1974), is an H II region associated with the molecular cloud L1204. In the rest of the paper, we will use S140 to refer to the whole cloud. The B0V star HD 211880 illuminates this cloud from the southwest side to create the visible H II region, an ionization front, and a bright PDR that has been studied extensively. For a picture that shows the CO emission in relation to the ionization front and exciting star, see Fig. 1 of Zhou et al. (1994). Northeast of the bright PDR lies the most prominent dense core (hereafter referred to as the S140 dense core) associated with the cloud. Numerous studies have been carried out on this cloud, e.g., Blair et al. (1978), Tafalla, Bachiller, & Martín-Pintado (1993), Plume, Jaffe, & Keene (1994), Emery et al. (1996), and Timmermann et al. (1996). The FUV radiation at the ionization front provided by HD 211880 is about 150 times Habing’s mean interstellar radiation field (Keene et al. 1985; Habing 1968). The S140 cut, specified in Table 1, is far enough ($\sim 20'$) from HD211880 to have a low FUV radiation field ($G_0 \sim 15 - 60$, §4.1, 4.3) and modest visual extinction ($A_V \sim 15$, §4.2).

2. OBSERVATIONS & DATA REDUCTION

² ISO is an ESA project with instruments funded by ESA Member States (especially the PI countries: France, Germany, the Netherlands and the United Kingdom), with the participation of ISAS and NASA.

We have observed the S140 cut with the Caltech Submillimeter Observatory (CSO³) and ISO. From the CSO, we collected data on transitions of ¹²CO and other CO isotopes, the neutral carbon [C I] ³P₂ → ³P₁ transition (hereafter [C I]), and the HCO⁺ *J* = 3 → 2 line (see details in § 2.1). We use these lines to determine column density of the inner part of the cloud and to constrain the density. We used ISO to observe the [C II] and [O I] lines along the cut (see details in § 2.2), which will help us to determine the *G*₀ and density of the cloud, as well as the incident FUV radiation intensity on the clouds. Finally, we observed rotational transitions of H₂ with ISO at selected positions (§ 2.2).

Different off-cloud positions have been used for the ISO and CSO observations, based on the IRAS 100 μm map and the CO emission (Table 1). The ISO Off position had to be chosen farther away from the S140 cut than the CSO Off position, because of the greater extent of the far-infrared continuum. The CSO Off position was used in position-switched observations, but the ISO Off position was observed in the same way as the on-cloud positions but with longer integrations, in order to measure the [C II] and [O I] lines from the general background and establish appropriate baseline intensities.

2.1. CSO Observations

Various molecular lines and the [C I] line were observed using the CSO, with parameters listed in Table 2. Most of the data were taken with a re-imaging device installed on the telescope so that the effective aperture was 1–2 m, depending on the frequency and the run (Plume & Jaffe 1995). The beam size with the re-imager installed, listed in Table 2 for each run, was 2′–3′ and is referred to as the “big beam”. Beam sizes of the big beam in Table 2 are accurate to better than 10%. Since our object is extended, the exact beam size is not critical. The [C I] line was observed with the full dish (when the re-imager was unavailable), in the mode of “On-The-Fly Mapping”; then the data were smoothed to 120″ to match the big beam. The pointing and the main-beam efficiency were obtained by observing the available planets and the Moon. For the full dish observations, the pointing uncertainty was less than 5″; with the re-imager, it was no more than 30″.

The CSO facility SIS receivers were used for all observations. The backend was a 1024-channel acoustic-optical spectrometer, with a bandwidth of 50 MHz. The typical single-sideband system temperature was 300 K for the 230 GHz band, 1300 K for the 345 GHz band, and 4000 K for the 490 GHz band. Observations were done with position switching between the on- and the off-source positions. The data are presented on the T_A^{*} scale. The rms noise is not uniform for the CSO data, because of different integration times, weather conditions, and instrument performance. At some positions, for some less abundant species, data were not taken because of extremely weak emission predicted from the more abundant isotopes and the usual abundance ratios. Repeated observations showed that uncertainties of the results are less than 30%.

2.2. ISO Observations

Parameters for the ISO observations are in Table 3. Information about ISO can be found in Kessler et al. (1996). We used the Long-Wavelength Spectrometer (LWS; Clegg et al. 1996; Swinyard et al. 1996) to observe the [C II] and [O I] lines in the LWS02 mode at 16 positions along the S140 cut. For each line at every position, multiple scans were obtained; each scan had 19 samples covering a width of 5 spectral resolution elements. Each sample had an integration time of 0.4 sec. Particle hits caused a number of bad scans, resulting in a significant reduction of usable data. Three selected positions from the S140 cut were observed in the [C II] and [O I] lines with longer integrations. The ISO Off position of S140 was also observed in the [C II] and the [O I] lines. The data presented here have been processed through the Off-Line Processor Version 8.7 (OLP 8.7), and the line fluxes were extracted by using the ISO Spectral Analysis Package Version 1.6a (ISAP 1.6a), calculated under the assumption that the sources were point sources. Processing consisted of removing bad scans and obvious glitches and, in a few cases, DC offsetting the continuum to be closer to that of the other scans. The points were then averaged together using 2.5σ clipping and fitted with a line and baseline fit. The quoted errors are those given by the fit. Because the standard calibration assumes a point source and, in the region we mapped, the line emission is more extended than the beam, we multiplied these fits by 0.84 for the 63 μm [O I] line and 0.59 for the 157 μm [C II] line, using Table 4.10 of Gry et al. (2001). We then converted to surface brightness, using beam solid angles listed in Table 4.14 of Gry et al. (2001). The relevant detectors are SW3 ([O I]) and LW4 ([C II]), resulting in beam solid angles of 1.30 × 10⁻⁷ for [O I] and 6.65 × 10⁻⁸ for [C II]. The [O I] solid angle is smaller than the nominal ISO beamsize of 1.6′ but considerably larger than the diffraction limit. The [C II] beamsize is slightly larger than the diffraction limit at 158 μm. The point source fluxes were multiplied by the following factors to get surface brightness in ergs s⁻¹ cm⁻² sr⁻¹: [O I] 6.46 × 10¹³; [C II] 8.87 × 10¹³. In addition to our own cut through the cloud, we have reprocessed the LWS data taken toward the bright PDR near the far-infrared peak in S140 itself, originally taken for the program of Emery et al. (1996, TDT 09101820 in the ISO Data Archive) and for another program (TDT’s 82301120, 122, and 123) using the same corrections as for the data from our own program.

Because the LWS has ten detectors, we also obtained undersampled far-infrared continuum scans covering from about 43 μm to 175 μm from the detectors that were not on the lines. However, because of dark current uncertainty for the bands shorter than 100 μm and the fringing problem for the bands longer than 100 μm (Swinyard et al. 1996), we could not make accurate measurements of the far-infrared continuum from the ISO scans. Therefore in this work, we will use the IRAS measurements to constrain the far-infrared emission.

The low-lying pure-rotational H₂ *J* = 2 → 0 S(0) line at 28.218 μm and the *J* = 3 → 1 S(1) line at 17.035 μm were observed with the ISO-SWS in the AOT02 mode (de Graauw et al. 1996). Typical integration times were ~100 s per line, in which the 12 detectors were scanned once over the 28.05–28.40 and 16.96–17.11 μm ranges

³ CSO is operated by the California Institute of Technology under funding from the National Science Foundation, contract 96-15025.

around the lines. The $J = 5 \rightarrow 3$ S(3) $9.66 \mu\text{m}$ and $J = 7 \rightarrow 5$ S(5) $6.91 \mu\text{m}$ lines were measured in parallel with the S(0) and S(1) lines, respectively. The spectral resolving power for point sources is 2000 (150 km s^{-1}) at $28 \mu\text{m}$, 2400 (125 km s^{-1}) at $17 \mu\text{m}$, 2280 (130 km s^{-1}) at $9.7 \mu\text{m}$ and 1550 (195 km s^{-1}) at $6.9 \mu\text{m}$. The SWS apertures are $20'' \times 27''$ at S(0), $14'' \times 27''$ at S(1), and $14'' \times 20''$ at the S(3) and S(5) lines. Since the SWS beam is considerably smaller than the LWS beam, three positions separated by $30''$ in RA were observed for each of the three LWS positions and averaged to produce an intensity for comparison to the LWS data.

The H_2 lines from translucent clouds are predicted to be weak and close to the sensitivity limit of the SWS instrument. At this level, noise induced by charged-particle impacts on the detectors plays a large role. By good fortune, these particle hits were exceptionally low during the orbit in which the H_2 data for S140 were taken so that the quality of the data ($\sim 0.2 \text{ Jy rms}$ at $28 \mu\text{m}$) is comparable to that commonly obtained in much longer integration times. The H_2 S(0) and S(1) lines were detected with the standard pipeline reduction, but special software designed to handle weak signals in combination with the standard Interactive Analysis Package was used for improvements in the signal-to-noise ratio. This technique also yields a possible detection of the S(3) line at one position. The details and justification of the methods used in the software are described by Valentijn & Thi (2000) and Thi et al. (2001). Because the mid-infrared continuum emission is weak, $< 3 \text{ Jy}$, the data do not suffer from fringing effects caused by an inadequate responsivity function correction. However, the uncertainties are dominated by the removal of the fluctuating dark current (see Leech et al. 2001), leading us to adopt a calibration uncertainty of $\sim 30\%$, which is propagated in the analysis.

3. OBSERVATIONAL RESULTS

Observational results from the CSO and ISO are presented in Tables 4–7. Spectra of $^{12}\text{CO } J = 2 \rightarrow 1$, $^{13}\text{CO } J = 2 \rightarrow 1$, $\text{C}^{18}\text{O } J = 2 \rightarrow 1$, and the [C I] line at two selected positions are shown in Figure 2. Figure 3 shows the spectra of the [C II] and the [O I] lines, averaged over the whole S140 cut, along with the H_2 S(0) and S(1) lines averaged over the three LWS positions where SWS observations were made.

Two velocity components of $V_{\text{LSR}} \sim -7.5 \text{ km s}^{-1}$ and $V_{\text{LSR}} \sim -10.5 \text{ km s}^{-1}$ are clearly seen in the CSO data along the S140 cut. In Table 4, results for each component are given when applicable. The line widths (FWHM) of the $\text{C}^{18}\text{O } J = 2 \rightarrow 1$ transition of both components are around 1.3 km s^{-1} , implying a Doppler parameter, $b = 0.78$, where b is the $1/e$ half-width of the line. The first component is very close to the velocity observed at the S140 dense core. Therefore the molecular gas with this velocity is likely to be the cloud extension of the S140 dense core. The second component, strongly peaking around $(774'', 0)$ (Table 4) for the [C I] line and the lines of ^{12}CO and other CO isotopes, is the same as that of core F identified in CS $J = 1 \rightarrow 0$ and NH_3 (1,1) and (2,2) by Tafalla et al. (1993). This dense core, apparently active in star formation with an associated IRAS source and outflow, is centered at $(954'', -60'')$ (relative to the reference point

of this work in Table 1) and extends about $2' \times 2'$ in NH_3 (1,1). We distinguish the emission in this component from the cloud by referring to it as core F; the first component is referred to as the cloud. We define the mean emission in core F as the average of the 5 positions with offsets in α between $576''$ and $972''$, using only the -10.5 km s^{-1} component. These positions include all with obvious effects from core F. The mean emission from the cloud is the mean of emission from all positions in the -7.5 km s^{-1} component added to the mean emission from the -10.5 km s^{-1} component outside that range of α . We add the two components for comparison to the ISO observations, which are not spectrally resolved.

Table 5 presents results of the $\text{HCO}^+ J = 3 \rightarrow 2$ line at selected positions. At $(774'', 0)$, we detected a 0.2 K line of $\text{HCO}^+ J = 3 \rightarrow 2$ with the re-imager. Following this detection, the full dish was used to map an area of $300'' \times 300''$ centered at $(774'', 0)$. The small-beam map revealed that the emission is clumpy. The strongest clump is close to the peak of NH_3 (1,1) detected by Tafalla et al. (1993) (see Figure 1). In Table 5 we list the small-beam results at the peak position. Big-beam observations of the $\text{HCO}^+ J = 3 \rightarrow 2$ line at other positions did not result in any detection up to the standard deviations given in Table 5.

Measurements of the [C II] and [O I] lines are given in Table 6, as is the ratio, $[\text{O I}]/[\text{C II}]$, and the IRAS continuum intensities at $60 \mu\text{m}$ and $100 \mu\text{m}$. Line measurements from the combined data set of all 16 positions along the S140 cut (Avg(16-pos)), at the S140 PDR peak position, and at the ISO off position are also given in the table. The 1σ uncertainties come from the Gaussian fits performed by ISAP. These uncertainties are appropriate in evaluating the reliability of spatial variations in line strengths and line ratios. In comparisons of the absolute values of these quantities to theoretical models, the overall calibration uncertainty provides a more useful assessment of the significance of the results. The overall uncertainty results from a combination of model uncertainties for the primary calibrator (Uranus), variations in the detector dark current, and uncertainties in the value of the system solid angle at each wavelength (Swinyard et al. 1998). Considering the various correction factors and their uncertainties, we adopt a value of 30% for this overall uncertainty.

Figure 4 shows the positional variations along the S140 cut of the $^{13}\text{CO } J = 2 \rightarrow 1$ and [C I] lines (of two velocity components separately), the [C II] and [O I] lines, and the intensity of the IRAS $100 \mu\text{m}$ continuum. The dotted lines for the panels of the [C II] and [O I] lines mark the line measurements of all the data combined of the 16 positions (Avg(16-pos) in Table 6). Clearly, the [C II] and [O I] lines and the $100 \mu\text{m}$ continuum are quite flat over most of the S140 cut, while the $^{13}\text{CO } J = 2 \rightarrow 1$ line displays more than a factor of 10 variation in both velocity components, and the [C I] varies by a factor of 4. The $^{12}\text{CO } J = 2 \rightarrow 1$, $^{13}\text{CO } J = 3 \rightarrow 2$, and $\text{C}^{18}\text{O } J = 2 \rightarrow 1$ show strong spatial variation similar to the $^{13}\text{CO } J = 2 \rightarrow 1$ line. In contrast, the average [C II] and [O I] fluxes of the 16 positions (Avg(16-pos)) agree with the measurements at each individual position within 40%. Thus, core F is simply not apparent at all in the [C II], [O I], or far-infrared emission. Therefore, we will use the [C II] and [O I] data averaged

over all 16 positions as representative of the cloud. Core F is also not noticeable in the more limited H₂ data (Table 7).

The average [C II] and [O I] intensities are 8.66×10^{-5} and 1.35×10^{-5} erg s⁻¹ cm⁻² sr⁻¹ respectively, and the average line ratio [O I]/[C II] is 0.16 ± 0.04 . If we subtract the emission at the ISO-OFF position from the mean values, the intensities for [C II] and [O I] are 6.97×10^{-5} and 0.89×10^{-5} ergs s⁻¹ cm⁻² sr⁻¹, with a ratio of [O I]/[C II] of 0.13. These numbers are very different from the S140 bright PDR, where the ratio of [O I]/[C II] is 1.55 ± 0.10 , based on our reduction of the archival data, using an analysis like that used for our own data. For the peripheral regions, [C II], rather than [O I], is the primary coolant.

The intensities of the H₂ lines are roughly constant at $\sim 10^{-5}$ erg s⁻¹ cm⁻² sr⁻¹ at the three positions (Table 7). In addition, the excitation temperature between $J = 3$ and $J = 2$ is also constant within uncertainties at ~ 100 K. The constancy of intensity and temperature is rather remarkable because one position is toward core F and the other two are positions near the ends of the cut, without emission from lines tracing molecular gas of moderate density (cf. Table 4). Clearly, the H₂ emission has the same pattern of constancy as the [C II] and [O I] lines and traces the gas in the PDR.

The H₂ S(3) line is only tentatively detected at one position, with an excitation temperature between $J = 5$ and $J = 3$ of ~ 350 K. The non-detections at the other positions give a comparable upper limit on the temperature.

4. MODELING AND DISCUSSION

In this section, we will attempt to reproduce the observations by using both published models and our own PDR models. The most important free parameters in the modeling are the FUV radiation intensity, the total extinction, and the volume density. Therefore, we will first constrain the FUV intensity (§ 4.1) and the extinction and density (§ 4.2). Then we will compare the predicted [C II] and [O I] line intensities with the ISO observations in § 4.3, 4.4.

4.1. The FUV Radiation Field Estimated from the Far-infrared Continuum

Because dust grains absorb most of the FUV photons incident on the cloud and most of that energy is re-emitted in the form of far-infrared continuum, the intensity of the FUV radiation can be inferred from the far-infrared continuum. Hollenbach et al. (1991) presented model predictions of the far-infrared continuum intensities at 100 μ m and 60 μ m for a range of incident FUV intensity.

From Table 6 and Figure 4, the IRAS 100 μ m and 60 μ m intensities are quite uniform along most of the S140 cut except at Positions 15–16 for 60 μ m and the Positions 13–16 for 100 μ m, where the intensities are lower. Therefore we use the intensities averaged over positions 1–13 and the intensity at position 16 to estimate a range of values for the ultraviolet intensity. The continuum intensities at the ISO Off position have been subtracted to yield $I(60) = 30 - 50$ MJy sr⁻¹ and $I(100) = 100 - 180$ MJy sr⁻¹. Assuming a λ^{-1} dust emissivity, the total far-infrared intensity is about 6×10^{-3} ergs s⁻¹ cm⁻² sr⁻¹.

These intensities and a λ^{-1} dust emissivity yield a dust temperature of (28 ± 2) K, near the constant value of 27 K

reached for $G_0 < 160$, when effects of transient heating of small grains/PAHs by single photons are included (Hollenbach & Tielens 1995). Therefore, the 60 μ m continuum intensity in this region is probably strongly affected by small grains. Based on Fig. 18 of Hollenbach et al. (1991), we used the 100 μ m intensity to estimate the strength of the ultraviolet field as $G_0 = 40 - 60$. As noted by Kaufman et al. (1999), these values assume that the FUV impinges only on one surface of the cloud. If the cloud is heated from both sides, then the values of G_0 appropriate to one surface would be 20 - 30. The assumption here is that the cloud is optically thin to the far-infrared continuum. Given the uncertainties in the fraction of the grain heating caused by FUV photons, we estimate G_0 in the range, 15–60. The enhancement factor of the radiation field I_{UV} with respect to the standard field given by Draine (1978) is 1.71 times smaller than G_0 , $I_{UV} = G_0/1.71$ (Draine & Bertoldi 1996).

4.2. Column Density and Density Regime

The mean integrated intensity of C¹⁸O $J = 2 \rightarrow 1$ for the cloud component is 0.54 K km s⁻¹. From Table 4, the typical excitation temperature of ¹²CO is about 10 K. Assuming that the C¹⁸O $J = 2 \rightarrow 1$ line is optically thin and in LTE, we calculate analytically the total column density of C¹⁸O to be $\leq 1.3 \times 10^{14}$ cm⁻². The empirical relations of Frerking, Langer, & Wilson (1982) on ρ Oph yield a visual extinction, $A_V = 3.4$ mag, and a total column density of H nuclei of 5×10^{21} cm⁻². Assuming the cloud is spherical and the angular size of the cloud along the S140 cut is roughly 15', the linear size of the depth of the cloud would be 1.2×10^{19} cm (4 pc) at a distance of 910 pc. Therefore, the average density along the S140 cut would be 800 cm⁻³. The assumption of LTE is not valid at such a low density. Models of excitation, including trapping with LVG codes, indicate that the C¹⁸O populations at such low densities are far from LTE. A more self-consistent solution is a density around 2000 cm⁻³ and a column density of C¹⁸O of 2.0×10^{15} cm⁻², yielding $A_V = 16$. The ratio of $J = 2 - 1$ to $J = 3 - 2$ lines of ¹³CO is roughly consistent with a density of 2000 cm⁻³, and the non-detection of HCO⁺ $J = 3 - 2$ outside core F limits the density to $n < 10^4$ cm⁻³ for typical abundances in translucent clouds and $T_K = 10 - 20$ K. Similar considerations applied to the position of core F (774,0) lead to estimates of $A_V = 25$ mag and, using a size of 3', a mean density of 10^4 cm⁻³.

Considering the uncertainties in these estimates, the likely uncertainties in column density and density are factors of 2 and 3, respectively. A direct comparison between PDR models and our data will be given in §4.4, which supports these simple estimates.

4.3. Comparison to Published PDR Models

We first compare our results to the published grid of PDR models by Kaufman et al. (1999). These calculations incorporated new collision rates for fine-structure lines and H₂, new PAH heating and chemistry, and lower gas-phase abundances for oxygen and carbon (Savage & Sembach 1996). They include regions of low FUV and low density, which seem to be appropriate for our situation. The calculations employed a turbulent broadening of 1.5 km s⁻¹, about twice what we infer, but Kaufman

et al. argue that the results are not too sensitive to this parameter.

We first consider the constraints from the two atomic species, [C II] and [O I]. From Fig. 4 of Kaufman et al., the mean ratio of [O I]/[C II] of 0.16 ± 0.4 constrains $G_0 < 20$. This is at the low end of the range inferred in §4.1, even if we assume the cloud is heated from both sides. At this G_0 , the only solution for density is $n \sim 300$, lower than the values inferred in §4.2. For lower G_0 , the solutions for n bifurcate into lower and higher values. For example, at $G_0 = 10$, there are solutions for $\log n = 2.0$ or 3.3 . The latter are more consistent with the LVG modeling of $\text{C}^{18}\text{O } J = 2 \rightarrow 1$. The [C II] emission by itself (Fig. 3 of Kaufman et al.), is less diagnostic, but roughly consistent with the ranges implied by the ratio.

Are these low values of G_0 consistent with the far-infrared emission? They are substantially below the estimates from §4.1. Our ratio of intensities of the sum of the [O I] and [C II] lines to the total far-infrared intensity, 1.7×10^{-2} , is close to the highest values found by Kaufman et al. (1999). In fact, the ratio of line to continuum of the cloud in S140 may exceed the maximum in their models, if indeed the cloud is heated from both sides.

What about the [C I] data? The mean for the cloud, summing the two components as for the C^{18}O data, and correcting for efficiency, is $1.3 \times 10^{-6} \text{ ergs s}^{-1} \text{ cm}^{-2} \text{ sr}^{-1}$. Comparing to Fig. 7 of Kaufman et al., this value favors very low G_0 . To get G_0 up to even 15 requires $n \sim 100$. For the conditions that match the other lines, the [C I] prediction of Kaufman et al. is too high by a factor of 3–4.

Given reasonable uncertainties, the mean cloud data require quite low values of G_0 and n , with most likely values of $G_0 \sim 15$ and $n \sim 1000$. These are both lower than our initial guesses, even if the cloud is heated from both sides. For this range of conditions, the “surface temperature” of the PDR, plotted in Fig. 1 of Kaufman et al., will lie between 100 and 200 K. This is the maximum temperature that should apply to the region of H_2 emission, if collisions dominate the H_2 excitation. The excitation temperatures of H_2 (Table 7) are consistent with this range of temperatures, but the absolute intensities are difficult to reproduce (§6).

Comparison of the Kaufman et al. results with those of other models in the literature (e.g., Le Bourlot et al. 1993, Roueff, private communication) and our own models (e.g., Jansen et al. 1995, Spaans & van Dishoeck 1997, Spaans, private communication), shows good agreement for the [C II] intensities but variations of factors of two in the [O I] intensities depending on the temperature structure, radiative transfer treatment and geometry of the source. Thus, the range in inferred G_0 and n could be somewhat larger, but the conclusion that both are low holds firm.

The region of the core F emission is clearly denser than that of the cloud, yet core F is not apparent in either far-infrared lines or continuum. The emission from the [C II] line may be quite independent of density up to about $n \sim 10^4 \text{ cm}^{-3}$, in the allowed range of G_0 ; however, the [O I] line should increase with density. From Fig. 4 of Kaufman et al. (1999), the ratio of [O I]/[C II] should increase to about 1 for $n = 10^4$ and G_0 in the range that fits our data. To keep the ratio below 0.3 would require

$G_0 \sim 1$. That is, core F would have to be shielded from the ambient FUV field. Interestingly, the [C I] emission does see core F in the -10.5 km s^{-1} line. Either that component is not completely shielded or the enhanced [C I] is caused by some internal source that does not affect the far-infrared line and continuum emission.

4.4. Comparison to PDR-Monte Carlo Models

To check the effects of radiative transport, different Doppler broadening, and metal abundance at these low values of G_0 and n , we ran our own models for the part of parameter space indicated in the last section. We used our own PDR code, an updated version of the code described by Jansen et al. (1995) to calculate abundances of relevant species as a function of depth into the cloud. We then fed the results into a Monte Carlo code (Hogerheijde & van der Tak 2000) to calculate excitation and radiative transport. Einstein A values of [C II] and [O I] were taken from Tielens & Hollenbach (1985a) and Galavis et al. (1997), respectively. In going from the PDR code to a spherical Monte Carlo code, one doubles the column density, so the PDR models were run for $A_V = 9$, yielding a total extinction through the cloud of 18 mag. We ran models for Doppler parameters from 0.5 to 2.0. The integrated intensities were generally insensitive to this parameter. Two sets of values for metal abundances were used: normal abundances are those listed by Jansen et al. (1995) in their Table 2 for the ζ Oph diffuse cloud; “low metals” corresponds to decreasing all abundances other than C, N, and O by a factor of 10. The most important species is S, which is thought to be quite depleted in molecular clouds compared to translucent clouds.

The results showed that the radiative transport of [O I] is indeed quite sensitive to the input parameters because it is very subthermally excited at these low densities, but quite opaque ($\tau \sim 10$ for models that fit the data well). At very low values of G_0 and n , the [O I] line predicted by the Monte Carlo cloud can be considerably stronger than that predicted by the PDR code alone, after accounting for the doubling of the column density. The differences seem to be partially in the handling of the radiative transport and partly in the geometry. Calculations that calculate the temperature self consistently in spherical geometry produce even larger effects (M. Spaans, personal communication).

Among a grid of models, the best fit was obtained for a model with $G_0 = 17$ and $n = 1000$ and low metals. This model reproduced the C^{18}O line strength, indicating that the extinction estimate from §4.2 was about right. The ratio of $^{13}\text{CO } J = 3 \rightarrow 2 / ^{13}\text{CO } J = 2 \rightarrow 1$ was about 50% lower than the observations in this model, while models with $n = 3000$ gave ratios higher than observed and $^{13}\text{CO } J = 2 \rightarrow 1$ lines about a factor of 2 stronger than observed. The $\text{HCO}^+ J = 3 \rightarrow 2$ line produced by this model is about 1.5 times our RMS noise, still consistent with the observations, while the model with $n = 3000$ would produce a 10σ detection. The HCO^+ abundance and thus the $\text{HCO}^+ J = 3 \rightarrow 2$ line are considerably enhanced in the case of low metals. Taken together, these results suggest that $n = 1000 \text{ cm}^{-3}$ is about right, but perhaps a bit low.

The best model gave a [C II] line in good agreement with observations and an [O I] line about 40% too strong.

Higher values of G_0 or n greatly overproduced the [OI] line. These are in rough agreement with Kaufman et al., but the [C I] line predicted by our models is about a factor of 4 weaker than the line predicted by Kaufman et al., and our prediction agrees with the observations. Kaufman et al. note that their [C I] lines are stronger than in previous calculations because of inclusion of PAH chemistry in their models. While charge transfer from PAHs to C^+ to create C^0 is included in our models, the details may be different.

We use the results of the model with $G_0 = 17$ and $n = 1000$ in the next section.

5. TESTING PHOTOIONIZATION-REGULATED STAR FORMATION

Figure 5 shows the distribution of electron fraction ($x(e) \equiv n(e)/n$, with $n = 2n(H_2) + n(H)$) with extinction from the best fitting models from §4.4. The model with low metals fits the $C^{18}O$ data better and has slightly lower $x(e)$.

The timescale for ambipolar diffusion is:

$$t_{AD} \simeq 1.6 \times 10^{14} x(e) \quad \text{yrs},$$

where $x(e)$ is the electron abundance (McKee et al. 1993). Since the lifetime of molecular clouds is roughly 30 Myrs (Bash, Green, & Peters 1977), if t_{AD} exceeds this time, the region is effectively sterile as long as it remains magnetically sub-critical: it will be dissipated before it can form stars. By setting t_{AD} to 30 Myr, we find a threshold ionization fraction for star formation of $x(e) \simeq 2 \times 10^{-7}$. In Figure 5, the threshold $x(e) \simeq 2 \times 10^{-7}$ is reached at $A_V = 6$ mag for the low metal model and is not reached by the end of the high metal model at $A_V = 9$ mag. A cloud with a column density less than 6–10 mag will have little well-shielded ($x(e) < 2 \times 10^{-7}$) gas to form stars. Thus the ionization fraction in the region we are studying suggests that little star formation would be expected in the extended cloud, if photoionization-regulated star formation applies (McKee 1989).

Based on the above analysis, the localized core F along the S140 cut, with $A_V \sim 25$ mag, has substantial gas that is sufficiently well shielded ($x(e) < 2 \times 10^{-7}$) to allow star formation, which has been confirmed by the outflow around this core (Tafalla et al. 1993). This is consistent with McKee’s theory of photoionization-regulated star formation. In comparison, most of the molecular gas in the extended cloud, with $A_V \sim 16$ mag, has a $x(e) > 2 \times 10^{-7}$ and is unlikely to form stars, if subjected to FUV radiation from both sides of the cloud. Infrared studies to look for evidence of star formation in the peripheral region of S140 (away from core F) would be able to test this prediction and McKee’s theory.

Since the average extinction of molecular clouds in the Galaxy is about 7.5 mag (Larson 1981), according to the photoionization-regulated star formation model, most of the molecular gas will not form stars, leading to the low observed Galactic star formation rate. The sterility of much of the molecular gas is supported by the apparent absence of distributed populations of embedded stars in NGC 2023 (Li, Evans, & Lada 1997). The extinction in the peripheral region of that cloud, estimated from $^{13}CO J=1 \rightarrow 0$ emission is less than 10 mag, while that in the core is about 14 mag, just enough for shielding to decrease the ambipolar diffusion time. More recently, Carpenter (2000) has used

2MASS data to set upper limits on the distributed population in several clouds, again consistent with the result that star formation is largely confined to clusters forming in gas of higher than average extinction and density.

Of course, a long t_{AD} is only a necessary condition for the picture of photoionization-regulated star formation, not a sufficient one. The clouds must be magnetically subcritical as well. Crutcher (1999) has summarized the data on this topic, concluding that clouds were slightly supercritical, but he noted that the uncertainties allowed the clouds to be subcritical. Shu et al. (1999) have noted some corrections that make the clouds even closer to the critical boundary, and they suggested that observed clouds may be self-selected to be close to marginally critical.

6. THE H_2 EMISSION

The H_2 pure-rotational lines observed with the ISO-SWS provide a new test of the PDR models. Early ISO-SWS results have shown that H_2 lines up to $J = 7 \rightarrow 5$ S(5) are readily detected in traditional high density ($> 10^4 \text{ cm}^{-3}$), high G_0 ($> 10^3$) PDRs such as S140 at the position of the interface with the H II region (Timmermann et al. 1996, see review by Wright 2000). Those data give excitation temperatures for $J = 3 - 7$ of 400–700 K, much higher than expected from pre-ISO PDR models (Bertoldi 1997, Draine & Bertoldi 1999). Because of the high densities, the H_2 level populations are thermalized so that the H_2 intensities directly trace the temperature structure in the warm PDR layers. To remedy these discrepancies, Bertoldi (1997) suggested that either the photoelectric heating efficiency needs to be increased or that the H_2 formation rate on grains needs to be larger at high temperatures, shifting the $H \rightarrow H_2$ transition zone closer to the warm edge. Weingartner & Draine (1999) have calculated increased photoelectric heating efficiencies based on an enhanced dust-to-gas ratio in the PDR due to gas-grain drift, and Draine & Bertoldi (2000) have shown that such models can reproduce the H_2 observations of NGC 2023. Note that these comparisons include a factor of 5–10 enhancement of the models due to limb-brightening/geometry.

In the low-density, low G_0 regions of S140 studied here, the H_2 populations should be controlled by ultraviolet pumping rather than collisions, at least in the outer layers of the cloud. Moreover, enhanced efficiencies due to gas-grain drift should not play a role, nor should there be any geometrical effects in this face-on cloud. Thus, the ISO-SWS data should provide a test of the H_2 excitation in a different PDR regime (Thi et al. 1999). For the PDR parameters derived in the previous sections, $n \approx 1000 \text{ cm}^{-3}$ and $G_0 \approx 15$, standard low density PDR models such as those by Hollenbach et al. (1991) or le Bourlot et al. (1993) and our own models give H_2 excitation temperatures derived from the S(0) and S(1) lines of ~ 100 –200 K, consistent with our ISO data. However, these models underproduce the absolute H_2 intensities by at least an order of magnitude. The same conclusion was reached by Habart et al. (2000) and Kemper et al. (1999) for somewhat denser PDRs exposed to low G_0 . Habart et al. proposed to increase the H_2 formation rate on grains by more than a factor of 5 compared with the standard H_2 formation rate of $\sim 3 \times 10^{-17} \text{ cm}^3 \text{ s}^{-1}$ at 100 K (Jura 1975) to reproduce their observations.

If the H_2 formation rate in our S140 models is increased by a similar factor of 5, the comparison with observations is improved considerably, although the models still fall short by a factor of a few. Contributions from the far-side of the cloud could help to further reduce the discrepancies. Such an arbitrary, large increase of the H_2 formation rate is inconsistent, however, with the mechanism of the formation of H_2 by diffusion of physisorbed H atoms on silicate grains, which is effective only at very low temperatures (Pirronello et al. 1997). A mechanism in which H atoms are chemically attached to the grains and in which the second H atom lands directly on the attached H atom, the so-called Eley-Rideal mechanism (Herbst 2000) is one possible mechanism to explain a large formation rate at high temperatures. Porous (carbonaceous) grains and/or large PAH molecules appear to be the best candidate materials, but quantitative experiments and calculations on interstellar grain analogs at high temperatures are needed. In any case, an increase in the surface to volume ratio over the standard grain models may be needed to allow the high formation rates that seem to be necessary to explain our observations.

An alternative mechanism to increase the $\text{H}_2(J)$ populations has been proposed by Spaans (1995), Joulain et al. (1998) and Falgarone et al. (2000)—using the energy released by the dissipation of turbulence or by weak (few km s^{-1}) shocks. The observed H_2 intensities toward S140 are within a factor of a few of those predicted by Joulain et al. for a cloud with $n = 30 \text{ cm}^{-3}$. At densities typical for the periphery of S140, however, the turbulent model intensities should be reduced significantly. The models of Joulain et al. do not take ultraviolet pumping into account, which will enhance the populations of the higher J levels. Further development of these models and constraints from other observed species will be needed to test them fully.

It should be noted that the strengths of the S(0) and S(1) lines observed in the outskirts of S140 are comparable to those inferred from ultraviolet observations of H_2 in diffuse and translucent clouds. Consider as an example the recent FUSE results for the translucent cloud toward HD 73882 ($A_V=2.4$ mag) by Snow et al. (2000). The observed column densities in $J = 2, 3,$ and 5 translate into intensities of $2.1 \times 10^{-6}, 1.4 \times 10^{-5},$ and $1.7 \times 10^{-5} \text{ erg s}^{-1} \text{ cm}^{-2} \text{ sr}^{-1}$ for the S(0), S(1), and S(3) lines, respectively. The S(1) intensity is comparable to our observed values, but that of S(0) is lower and of S(3) higher. Indeed, the corresponding excitation temperatures for the $J = 2-7$ levels of $\sim 300 \text{ K}$ are larger than those of $\sim 100 \text{ K}$ found here for the $J = 2-3$ levels, although they are consistent with that found for the $J = 3-5$ levels at one position. More sensitive searches for the higher rotational lines of H_2 are needed to constrain its excitation and determine the relative roles of ultraviolet pumping, collisions, and the H_2 formation mechanism in establishing the level populations. FUSE studies of the H/ H_2 transition in well-characterized, low H_2 column density regions are also interesting to provide further constraints on the empirical H_2 formation rate in different environments using the analysis of Jura (1975).

In summary, the H_2 excitation temperatures and the widespread nature of the emission suggest a PDR origin, in which the H_2 lines arise from the outer warm layers. However, the absolute model intensities fall short by an

order of magnitude, unless the H_2 formation rate is enhanced significantly. Other explanations invoked for high-density PDRs, such as geometry or gas-grain drift, do not apply to these regions. Together with the results from ultraviolet observations, our results suggest that our understanding of the basic chemical processes involving H_2 is still incomplete.

7. LESSONS FOR OTHER GALAXIES

The [C II] 158 μm line and [O I] 63 μm lines are the dominant coolants of the interstellar gas in galaxies. A significant fraction of the [C II] emission from late-type galaxies arises in dense PDRs with some additional contributions from atomic gas not associated with molecular clouds. In the Milky Way, the [C II] emission fraction is about equally divided between PDRs associated with molecular clouds and neutral, purely atomic clouds (Petuchowski & Bennett 1993, Mochizuki & Nakagawa 2000, but see Heiles 1994 for a different view). PDRs contribute a larger fraction of the [C II] emission from galaxies with more active star formation (Crawford et al. 1985, Stacey et al. 1991) while, particularly in the outer parts of galaxies with lower star formation rates, purely atomic gas may contribute to the [C II] emission (Madden et al. 1993). The far-infrared continuum emission from galaxies comes primarily from the same PDRs, although, in the lowest luminosity spirals, optical emission from late-type stars may also contribute to the heating of dust in the molecular ISM (Smith et al. 1994) and something like half the far-infrared emission may come from purely atomic clouds (Mochizuki & Nakagawa 2000). It should be possible, in principle, to derive information about the physics of the neutral ISM in galaxies from the far-infrared continuum and fine-structure line measurements (Wolfire, Tielens & Hollenbach, 1990, Stacey et al. 1991, Carral et al. 1994, Lord et al. 1996, Malhotra et al. 2001).

Recent studies of starburst galaxies (Luhman et al. 1998) and of a range of lower luminosity spirals (Malhotra et al. 1997, 2001) have made much of an apparent “deficit” in the [C II] emission. In many of the starbursts and in a fraction of the spirals, the [C II]/FIR luminosity ratio lies as much as a factor of 10 below the canonical value (3×10^{-3}), more typical for late-type galaxies. Galactic photodissociation regions with high n or high G_0 can have [C II]/FIR ratios as low or lower than those of galaxies with the biggest [C II] deficits (e.g. Genzel, Harris, & Stutzki 1989). The [O I] line then provides a much larger fraction of the cooling power (cf. the values for the S140 cut and the S140 IRS 1 position in Table 6), and dust temperatures are higher. However, Malhotra et al. (2001) argue that the *total* fine structure emission ([O I] plus [C II]) is decreased substantially only if G_0/n is increased. This combination leads to highly charged grains and inefficient photoelectric heating (Tielens & Hollenbach 1985a, Bakes & Tielens 1994). Malhotra et al. (2001) considered but rejected a variety of explanations, concluding that high values of G_0/n in the emitting regions provide the best explanation for their sample of “normal” spirals.

Studies of far-infrared line emission from other galaxies have made use of the same models as adopted here, which assume a uniform incident radiation field and a single PDR density for the emitting material (Kaufman et al.

1999, Stacey et al. 1991, Wolfire et al. 1989). In addition to using simple models, we can gain insight into the nature of the regions in galaxies responsible for far-infrared fine-structure line emission by comparing galaxy PDR emission to emission from Galactic sources with an appropriate range of properties. The ISO observations of fine-structure line emission from other galaxies take in entire giant molecular cloud complexes and the nuclear regions of galaxies. They therefore contain contributions not only from the high excitation regions near OB stars but also from large regions with lower UV fields. With our measurements of the cut through the outer part of the S140 cloud, a comparison of Galactic and extragalactic fine-structure line emission can include a range of Galactic PDR conditions. Figure 6(a-c) reproduces the plots shown in Figures 1a, 5, and 8 of Malhotra et al. (2001) and shows the variation of $\text{Log}(L([\text{C II}])/L(\text{FIR}))$ (Fig. 6a), $L([\text{O I}])/L([\text{C II}])$ (Fig. 6b), and $\text{Log}((L([\text{C II}]) + L([\text{O I}]))/L(\text{FIR}))$ (Fig. 6c) versus $F_\nu(60\mu\text{m})/F_\nu(100\mu\text{m})$ for the 45 normal, star-forming galaxies in Table 7 of Malhotra et al. (2001). Figure 6 compares these data to the average values from our S140 cut and to typical values for high G_0 Galactic PDR sources (labeled H II for brevity), taken from Genzel, Harris, & Stutzki (1989) to be $L([\text{C II}])/L(\text{FIR}) = 8.5 \times 10^{-5}$, $L([\text{O I}])/L([\text{C II}]) = 5.8$, and $F_\nu(60\mu\text{m})/F_\nu(100\mu\text{m}) = 1.2$. Figure 6 clearly shows that the galaxies inhabit a part of parameter space that is different from either the S140 cut or the high G_0 PDR sources.

Because the galaxies generally lie between the points for the S140 cut and the high G_0 PDRs, we attempted to reproduce the galaxy observations by mixtures of the S140 cut and the high G_0 PDRs, indicated by the mixing line connecting these two points. The line represents parameters calculated by varying the contributions of the two connected Galactic components in proportion to the fraction of the [C II] emission contributed by each. It is not possible, however, to produce the observed positions of the galaxies in the figures with any linear combination of the S140 cut and the high G_0 PDRs. The result is similar if we use the emission from NGC 7023, representing reflection nebulae, instead of the H II regions. At all values of $F_\nu(60\mu\text{m})/F_\nu(100\mu\text{m})$, the mixture produces too much fine-structure line emission (in particular, too much [C II]), when compared to the galaxy sample. At a given value of $F_\nu(60\mu\text{m})/F_\nu(100\mu\text{m})$, for example, the value of $\text{Log}((L([\text{C II}]) + L([\text{O I}]))/L(\text{FIR}))$ observed for the galaxies lies on average 0.3 below the constructed mixture.

The results in Figure 6 show that one cannot produce the observed emission ratios in galaxies by simply combining regions like the S140 cut with regions of active star formation in our Galaxy. Malhotra et al. (2001) argued that models with high G_0/n can explain individual galaxies where the [C II] and [O I] is weak compared to the far-IR continuum. The systematically lower values of the galaxy ratios compared to positions along our mixing line, however, suggests that the conditions in heterogeneous clouds would not lead to appropriately weak line fluxes at a given value of $F_\nu(60\mu\text{m})/F_\nu(100\mu\text{m})$. Rather than focussing solely on the line to continuum ratio, it may be worthwhile to examine possible reasons why the $F_\nu(60\mu\text{m})/F_\nu(100\mu\text{m})$ ratio might vary. If that flux ratio increased less rapidly along the mixing line, the data could

be matched. Mixing very small amounts of high G_0 PDR emission has a big effect on $F_\nu(60\mu\text{m})/F_\nu(100\mu\text{m})$, while the effect on the line emission is more modest, as indicated by the tick marks on the mixing line that indicate where 90% and 50% of the [C II] emission comes from the S140 cut. Moderating the increase in $F_\nu(60\mu\text{m})/F_\nu(100\mu\text{m})$ as one mixes in small amounts of high G_0 PDR emission properties could allow the mixing line to pass through most of the points. This would require a component of emission from cooler dust. Lowering the 60–100 μm color temperature of the high G_0 PDRs from ~ 53 K to ~ 35 K (for a λ^{-1} emissivity law) could account for the difference. Even colder dust is common in the molecular clouds near the center of our Galaxy (Lis et al. 2001).

There are at least two possible causes for the cooler dust. The dust properties in the inner few kiloparsecs of galaxies, where most of the ISO emission arises, might differ significantly from those in nearby high G_0 Galactic PDRs. Alternatively, there might be a contribution from regions heated by cooler stars or from very opaque regions in molecular clouds. These regions would need to increase the fraction of the emission in the 100 μm IRAS band from 25% to 40% of the total far-infrared luminosity. Whichever reason is correct, observations of some regions in the inner part of our own Galaxy (G0.68-0.2, ISO data archive) find a far-infrared line to continuum ratio lower than for all the galaxies in the Malhotra sample, and yet the $F_\nu(60\mu\text{m})/F_\nu(100\mu\text{m})$ is only 0.2. A mixing line connecting G0.68-0.2 to the H II region/high G_0 PDR's would run below the bulk of the galaxies in Figures 6a and 6c. More complex 3-part mixtures of cold cloud edges like the S140 cut, cold inner galaxy clouds like G0.68 and warm H II regions could presumably fill the part of parameter space occupied by the galaxies from the Malhotra sample. Understanding the properties of inner Galaxy regions like G0.68 may provide further insight into the conditions in extragalactic PDRs.

8. SUMMARY

We have studied the peripheral region of the molecular cloud L1204/S140, where the FUV radiation and density are relatively low, using ISO to observe [C II], [O I], and H₂ lines, and the CSO to observe the submillimeter line of atomic carbon and millimeter emission lines of ¹²CO and other CO isotopes. We analyzed the results with published PDR models and our own PDR models, coupled to a Monte Carlo simulation code for radiative transfer. The important results from this work are:

1. We detected wide-spread [C II], [O I], and H₂ emission in the region. The [C II] and [O I] lines display much less spatial variation than [C I] and the lines from ¹²CO and other CO isotopes, which reveal the presence of a denser, shielded core that does not emit significantly in the [C II] and [O I] lines.
2. The average [C II] and [O I] intensities of the S140 cut are $(8.66 \pm 1.27) \times 10^{-5}$ and $(1.35 \pm 0.34) \times 10^{-5}$ ergs s⁻¹ cm⁻² sr⁻¹; the average line ratio ([O I]/[C II]) is 0.16 ± 0.04 . Therefore the [C II] line is the dominant cooling line in this region. This is quite different from what has been observed in the S140

bright PDR by ISO, where the ratio $[\text{O I}]/[\text{C II}]$ is 1.55 ± 1.10 .

3. Using the model predictions in Hollenbach et al. (1991) and the $100 \mu\text{m}$ IRAS flux, the FUV intensity G_0 for the region would be 40–60, in the situation of single-sided FUV radiation on the cloud. If the FUV impinges on both sides, the inferred $G_0 \sim 20 - 30$. Based on C^{18}O emission and simple LVG modeling, the density of the gas, $n \sim 1000 \text{ cm}^{-3}$, and $A_V \sim 16$. Conditions in the shielded core are different: $n \sim 1 \times 10^4 \text{ cm}^{-3}$, and $A_V \sim 25$.
4. The PDR models (both published and our own) indicate that the observed $[\text{O I}]$ intensity and the ratio $[\text{C II}]/[\text{O I}]$ are best reproduced with $G_0 \sim 15$ and $n \sim 1000 \text{ cm}^{-3}$. Our models, coupled to a Monte Carlo simulation of the radiative transfer, reproduce the observed $\text{C}^{18}\text{O } J=2 \rightarrow 1$ emission for $A_V \sim 18$ mag. These conditions are also consistent with the constraints on density from line ratios of ^{13}CO and HCO^+ . Our models also reproduce the observed $[\text{C I}]$ line, while the published models of Kaufman et al. (1999) overproduce this line. In this regime of n and G_0 , the $[\text{O I}]$ intensity is very difficult to model because it is extremely subthermal and also very opaque (the optical depth is 9–14). Trapping is very important in determining the emergent $[\text{O I}]$ intensity.
5. Quantitative analysis of the ionization structure and timescale for cloud collapse for the peripheral regions of S140 leads to conclusions consistent with a picture of photoionization-regulated star formation.
6. The detection of widespread H_2 rotational emission is not readily explained with standard PDR models and H_2 formation rates. Possible solutions include a substantial enhancement in the the H_2 formation rates or localized heating by weak shocks associated with turbulent decay.
7. While the emission in $[\text{C II}]$ and far-infrared continuum from other galaxies lies between the characteristics of the emission from the peripheral region studied here and regions of higher G_0 and n , simple mixtures of these regions are not able to reproduce the characteristics of the emission from other galaxies.

We thank the referee for a careful reading and for suggestions that improved the paper. We would like to extend our sincere thanks to the wonderful service by the ISO supporting staff at IPAC (S. Lord, S. Unger, D. Levine, L. Hermans especially) and at SRON Groningen (E. Valentijn and F. Lahuis in particular). We also thank the CSO staff members and E. Gregersen and K. Mochizuki for helping with the CSO observations. M. Spaans and D. Jansen provided useful discussions and help with PDR codes; E. Roueff provided data for comparison of PDR models. This research has made use of NASA’s Astrophysics Data System Abstract Service, the Simbad database, operated at CDS, Strasbourg, France, and the Online Services of

IRSKY and IBIS at IPAC, and the SkyView Online Service. WL was partially supported by a Continuing Fellowship and a David Bruton, Jr., Fellowship of the University of Texas, a Frank N. Edmonds, Jr. Memorial Fellowship and a David Alan Benfield Memorial Scholarship of the Department of Astronomy, the University of Texas. Work with the CSO re-imager was supported by NSF grant AST-9530695. The research was supported by NASA Grants NAG2-1055, NAG5-3348, and the State of Texas, NWO grant 614.41.003, a NWO Spinoza grant, and a NWO bezoekersbeurs.

REFERENCES

- Bakes, E. L. O. & Tielens, A. G. G. M. 1994, *ApJ*, 427, 822.
- Bash, F. N., Green, E., & Peters, W. L., III 1977, *ApJ*, 217, 464.
- Bertoldi, F. 1997, in First ISO Workshop on Analytical Spectroscopy, ESA SP-419 (Noordwijk: ESTEC), 67
- Bertoldi, F. & McKee, C. F. 1996, *Amazing Light: A Volume Dedicated to C. H. Townes on his 80th Birthday*, Ed. R. Y. Chiao (New York: Springer), p. 41.
- Bertoldi, F., & McKee, C.F. 1997, *Rev. Mex. AA (Serie de Conferencias)*, 6,195
- Black, J. H. & Dalgarno, A. 1977, *ApJS*, 34, 405.
- Blair, G. N., Evans, N. J., II, vanden Bout P. A., & Peters, W. L., III 1978, *ApJ*, 219, 896 homepage.
- Carpenter, J. M. 2000, *AJ*, 120, 3139
- Carral, P., Hollenbach, D.J., Lord, S.D., Colgan, S.W.J., Haas, M.R., Rubin, R.H., & Erickson, E.F. 1994, *ApJ*, 423, 223
- Clegg, P. E. et al. 1996, *A&A*, 315, L38.
- Crampton, D. & Fisher, W. A. 1974, *Pub. Dom. Ap. Obs.*, 14, 12.
- Crawford, M.K., Genzel, R., Townes, C.H., & Watson, D., 1985, *ApJ*, 291,755
- Crutcher, R. M. 1999, *ApJ*, 520, 706
- de Graauw, T. et al. 1996, *A&A*, 315, L49.
- Draine, B. T. 1978, *ApJS*, 36, 595.
- Draine, B. T. & Bertoldi F. 1996, *ApJ*, 468, 269.
- Draine, B.T., Bertoldi, F. 2000, in *Molecular Hydrogen in Space*, ed. F. Combes and G. Pineau des Forêts (Cambridge University Press), p. 131.
- Draine, B. and Bertoldi, F. 1999, in *the Universe as seen by ISO*, eds. P. Cox, M.F. Kessler, ESA SP-427, p. 553.
- Emery, R., et al. 1996, *A&A*, 315, L285.
- Evans, N. J., II 1991, *Frontiers of Stellar Evolution*, Ed. D. L. Lambert (San Francisco: Astronomical Society of the Pacific), p. 45.
- Evans, N. J., II, *ARA&A*, 37, 311
- Falgarone, E., Verstraete, L., Hily-Blant, P., Pineau-des-Forêts, G. 2000, in *Molecular Hydrogen in Space*, ed. F. Combes and G. Pineau des Forêts (Cambridge University Press), p. 225.
- Federman, S. R., Cardelli, J. A., van Dishoeck, E. F., Lambert, D. L., & Black, J. H. 1995, *ApJ*, 445, 325.
- Frerking, M. A., Langer, W. D., & Wilson, R. W. 1982, *ApJ*, 262, 590.
- Galavis, M. E., Mendoza, C., & Zeippen, C. J. 1997, *A&AS*, 123, 159.
- Genzel, R., Harris, A.I., & Stutzki, J. 1989, in *Proc. 22nd ESLAB Symposium*, B. Kaldeich ed., ESA SP-290, 115
- Gry, C., et al. 2001, *The ISO Handbooks*, vol. IV (LWS)
- Habart, E., Boulanger, F., Verstraete, L., Pineau des Forêts, G., Falgarone, E., Abergel, A. 2000, in *ISO beyond the Peaks*, ESA SP-456, p. 103
- Habing, H. J. 1968, *Bull. Astr. Inst. Netherlands*, 19, 421.
- Heiles, C. 1994, *ApJ*, 436, 720
- Herbst, E. 2000, *Astrochemistry: From Molecular Clouds to Planetary Systems*, IAU Symposium 197, eds. Y.C. Minh and E.F. van Dishoeck (San Francisco: ASP), p. 147
- Hogerheijde, M. R., Jansen, D. J., & van Dishoeck, E. F. 1995, *A&A*, 294, 792.
- Hogerheijde, M. R., & van der Tak, F. F. S. 2000, *A&A*, 362, 697
- Hollenbach, D. J., Takahashi, T., & Tielens, A. G. G. M. 1991, *ApJ*, 377, 192.
- Hollenbach, D. J. & Tielens, A. G. G. M. 1999, *Rev Mod. Phys.* 71, 173
- Hollenbach, D. J. & Tielens, A. G. G. M. 1995, *The Physics and Chemistry of Interstellar Molecular Clouds*, Ed. G. Winnewisser & G. C. Pelz (Berlin: Springer), p. 164.
- Jansen, D. J., van Dishoeck, E. F., Black, J. H., Spaans, M. C., Sosin, C. 1995, *A&A*, 302, 223.
- Jansen, D. J., van Dishoeck, E. F., Keene, J., Boreiko, R. T., & Betz, A. L. 1996, *A&A*, 309, 899.
- Joulain, K., Falgarone, E., Pineau des Forêts, G., Flower, D. 1998, *A&A*, 340, 241
- Jura, M. 1975, *ApJ*, 197, 755
- Kaufman, M. J., Wolfire, M. G., Hollenbach, D. J., & Luhman, M. L. 1999, *ApJ*, 527, 795.
- Keene, J., Blake, G. A., Phillips, T. G., Huggins, P. J., & Beichman, C.A. 1985, *ApJ*, 299, 967.
- Kemper, C., Spaans, M., Jansen, D.J., Hogerheijde, M.R., van Dishoeck, E.F., Tielens, A.G.G.M. 1999, *ApJ*, 515, 649
- Kessler, M. F. et al. 1996, *A&A*, 315, L27.
- le Boulrot, J., Pineau des Forêts, G., Roueff, E., & Flower, D. R. 1993, *A&A*, 267, 233.
- Leech, K. et al. 2001, *The ISO Handbooks*, vol. VI (SWS)
- Li, W., Evans, N. J., II, & Lada, E. A. 1997, *ApJ*, 488, 277.
- Lis, D. C., Serabyn, E., Zylka, R., & Li, Y. 2001, *ApJ*, 550, 761
- Liseau, R. et al. 1999, *A&A*, 344, 342
- Lord, S.D., Hollenbach, D.J., Haas, M.R., Rubin, R.H., Colgan, S.W.J., & Erickson, E.F. 1996, *ApJ*, 465, 703
- Madden, S. C., Geis, N., Genzel, R., Herrmann, F., Jackson, J., Poglitsch, A., Stacey, G. J., & Townes, C. H. 1993, *ApJ*, 407, 579
- Malhotra, S. et al. 1997, *ApJ* 491, 27
- Malhotra, S. et al. 2001, *ApJ*, 561, 766
- McKee, C. F., Zweibel, E. G., Goodman, A. A., & Heiles, C. 1993, *Protostars and Planets III*, 327
- McKee, C. F. 1989, *ApJ*, 345, 782.
- Mochizuki, K., & Nakagawa, T. 2000, *ApJ*, 535, 118
- Petuchowski, S. J. & Bennett, C. L. 1993, *ApJ*, 405, 591
- Pirronello, V., Biham, O., Liu, C., Shen, L., Vidalu, G. 1997, *ApJ*, 483, L131
- Plume, R., & Jaffe, D. T. 1995, *PASP*, 107, 488.
- Plume, R., Jaffe, D. T., & Keene, J. 1994, *ApJ*, 425, L49.
- Pringle, J. E., Allen, R. J., & Lubow, S. H. 2001, *MNRAS*, 327, 663
- Savage, B. D. & Sembach, K. R. 1996, *ARA&A*, 34, 279
- Shu, F. H., Allen, A., Shang, H., Ostriker, E. C., & Yun, Z.-Y. 1999, *The Origin of Stars and Planetary Systems*, ed. C. J. Lada & N. D. Kylafis (Dordrecht: Kluwer), 193
- Smith, B.J., Harvey, P.M., Colome, C., Zhang, C.Y., Di Francesco, J., & Pogge, R.W. 1994, *ApJ*, 425, 91
- Snow, T.P. et al. 2000, *ApJ*, 538, L65
- Spaans, M. 1995, PhD Thesis, University of Leiden
- Spaans, M. & van Dishoeck, E. F. 1997, *A&A*, 323, 953.
- Stacey, G.J., Geis, N., Genzel, R., Lugten, J.B., Poglitsch, A., Sternberg, A., & Townes, C.H. 1991, *ApJ*, 373, 423
- Steiman-Cameron, T. Y., Haas, M. R., Tielens, A. G. G. M., & Burton, M. G. 1997, *ApJ*, 478, 261.
- Sternberg, A. & Dalgarno, A. 1989, *ApJ*, 338, 197.
- Swinyard, B. M. et al. 1996, *A&A*, 315, L43.
- Swinyard, B.M. et al. 1998, *Proc. SPIE*, 3354, 896
- Tafalla, M., Bachiller, R., & Martin-Pintado, J. 1993, *ApJ*, 403, 175.
- Tauber, J., Tielens, A. G. G. M., Meixner, M., & Goldsmith, P. 1994, *ApJ*, 422, 136.
- Thi, W. F. et al. 2001, *ApJ*, 561, 1074
- Thi, W.F., van Dishoeck, E.F., Black, J.H., Jansen, D.J., Evans, N.J., Jaffe, D.T. 1999, in *The Universe as seen by ISO*, eds. P. Cox & M.F. Kessler, ESA SP-427 (Noordwijk: ESTEC), p.767
- Tielens, A. G. G. M. & Hollenbach, D. J. 1985a, *ApJ*, 291, 722.
- Tielens, A. G. G. M. & Hollenbach, D. J. 1985b, *ApJ*, 291, 747.
- Timmerman, R., Bertoldi, F., Wright, C. M., Drapatz, S., Draine, B. T., Haser, L., & Sternberg, A. 1996, *A&A*, 315, L281.
- Valentijn, E. A., & Thi, W.F. 2000, *Experimental Astronomy*, 10, 215
- van Dishoeck, E. F. & Black, J. H. 1986, *ApJS*, 62, 109.
- van Dishoeck, E. F. & Black, J. H. 1988, *ApJ*, 334, 771.
- van Dishoeck, E. F. & Black, J. H. 1989, *ApJ*, 340, 273.
- Weingartner, J.C., Draine, B.T. 1999, in *The Universe as seen by ISO*, eds. P. Cox & M.F. Kessler, ESA SP-427 (Noordwijk: ESTEC), p. 783
- Wright, C.M. 2000, in *Astrochemistry: from Molecular Clouds to Planetary Systems*, IAU Symposium 197, eds. Y.C. Minh and E.F. van Dishoeck (San Francisco: ASP), p. 177
- Wolfire, W. G., Hollenbach, D., & Tielens, A. G. G. M. 1989, *ApJ*, 344, 770.
- Wolfire, M. G., Tielens, A. G. G. M., & Hollenbach, D. J. 1990, *its The Interstellar Medium in External Galaxies: Summaries of Contributed Papers* p 37-39 (SEE N91-14100 05-90), 37
- Zhou, S., Butner, H. M., Evans, N. J., II, Güsten, R., Kutner, M. L., & Mundy, L. G. 1994, *ApJ*, 428, 219
- Zuckerman, B., & Palmer, P. 1974, *ARA&A*, 12, 279

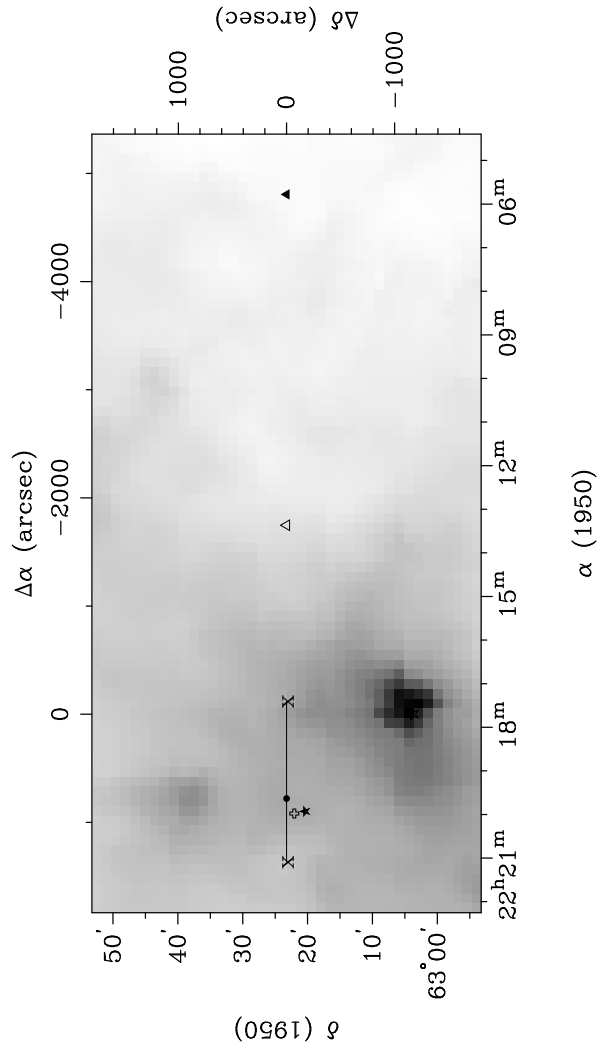


FIG. 1.— The S140 cut is marked as the line between two “X” symbols on the IRAS $100\ \mu\text{m}$ map of the region. Darker color indicates stronger $100\ \mu\text{m}$ emission. The open triangle is the CSO Off position, and the solid triangle marks the ISO Off. The open cross and the solid star are the centers of NH_3 (1,1) cores F and F’ identified by Tafalla et al. (1993). The F’ core has the same velocity ($V_{\text{LSR}} \sim -7.5\ \text{km s}^{-1}$) as the dense core at IRS1, while the F core is at a different velocity, $V_{\text{LSR}} \sim -10.5\ \text{km s}^{-1}$. The star marks the position of an IRAS source associated with the F core. The center of the ionization front is roughly located at $22^{\text{h}}\ 17^{\text{m}}\ 30^{\text{s}},\ 63^{\circ}\ 01'$; the exciting star for the ionization front is at $22^{\text{h}}\ 16^{\text{m}}\ 50^{\text{s}},\ 62^{\circ}\ 58'$. At the distance of S140, $1000''$ corresponds to 4.4 pc.

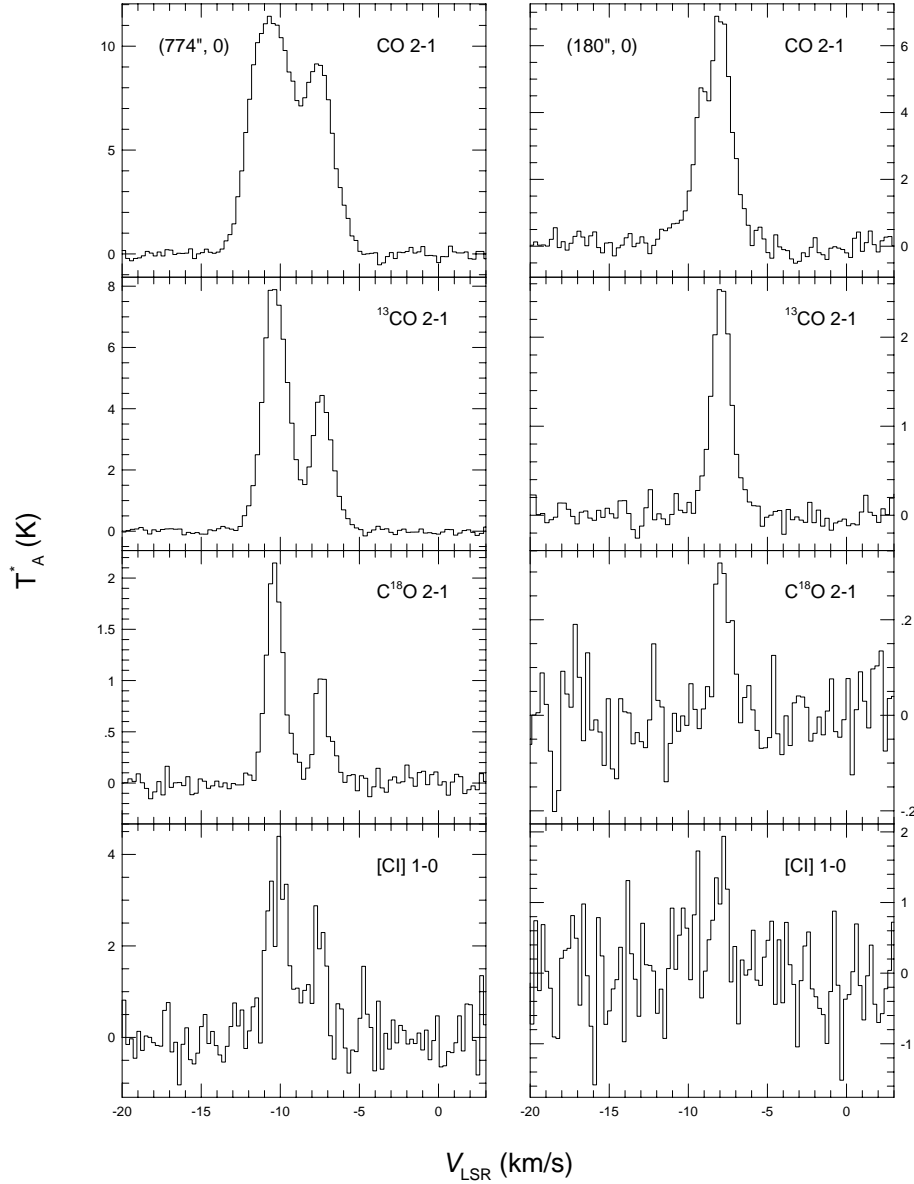


FIG. 2.— Spectra of $J=2\rightarrow 1$ lines of ^{12}CO , ^{13}CO , C^{18}O , and [C I] 492 GHz line at two selected positions. At the position (180'', 0), the line velocity (~ -7.5 km/s) is the same as that at the dense core at IRS1; thus the lines here are from the cloud extension of the dense core. At the position (774'', 0) two velocity components show up, one being the same as that of the dense core, another at about -10.2 km/s. The second component is from a distinct clump, as evidenced by the study of Tafalla et al. 1993

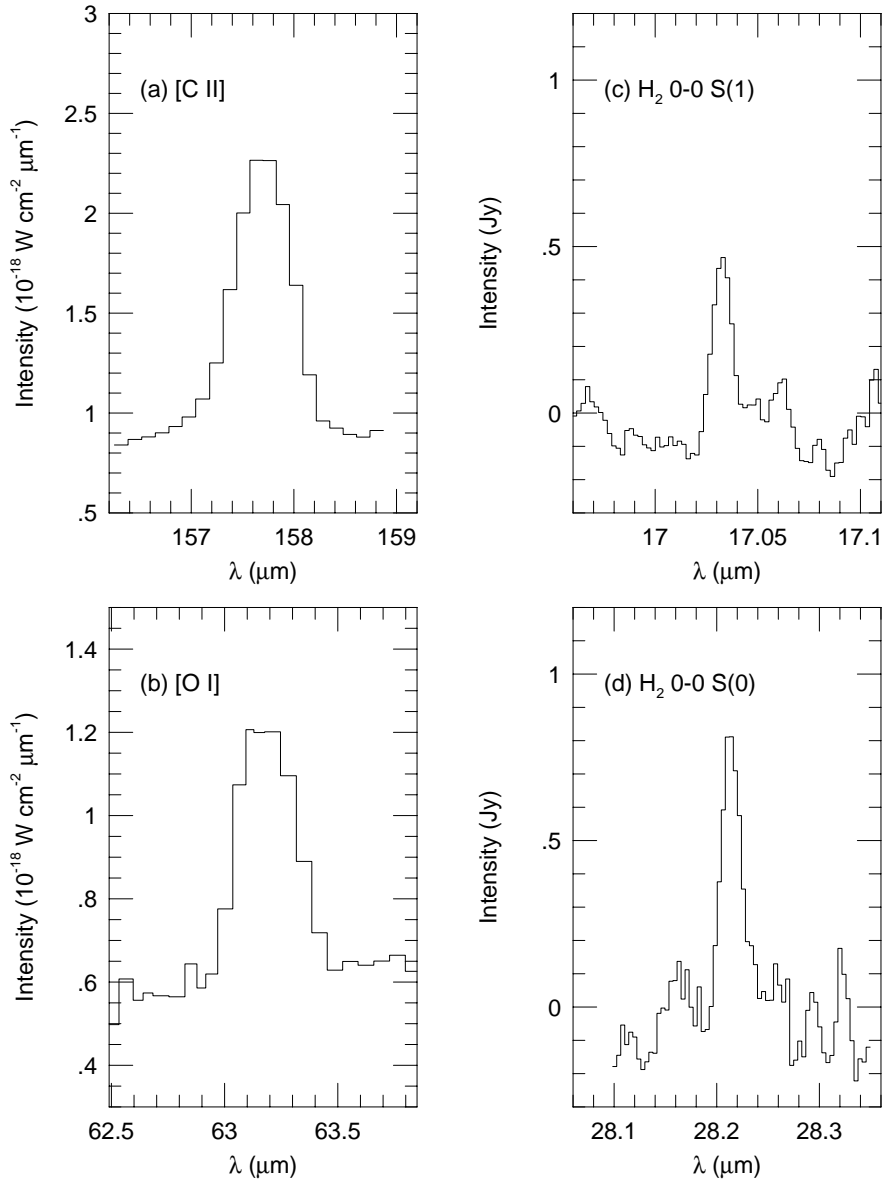


FIG. 3.— ISO spectra averaged along the S140 cut. None of the lines are spectrally resolved. The [C II] and [O I] spectra (panels a and b) are the averages of the 16 positions along the S140 cut, as listed in Table 6. The two H₂ spectra (panels c and d) are averaged over the 3 LWS positions observed with SWS (Table 7).

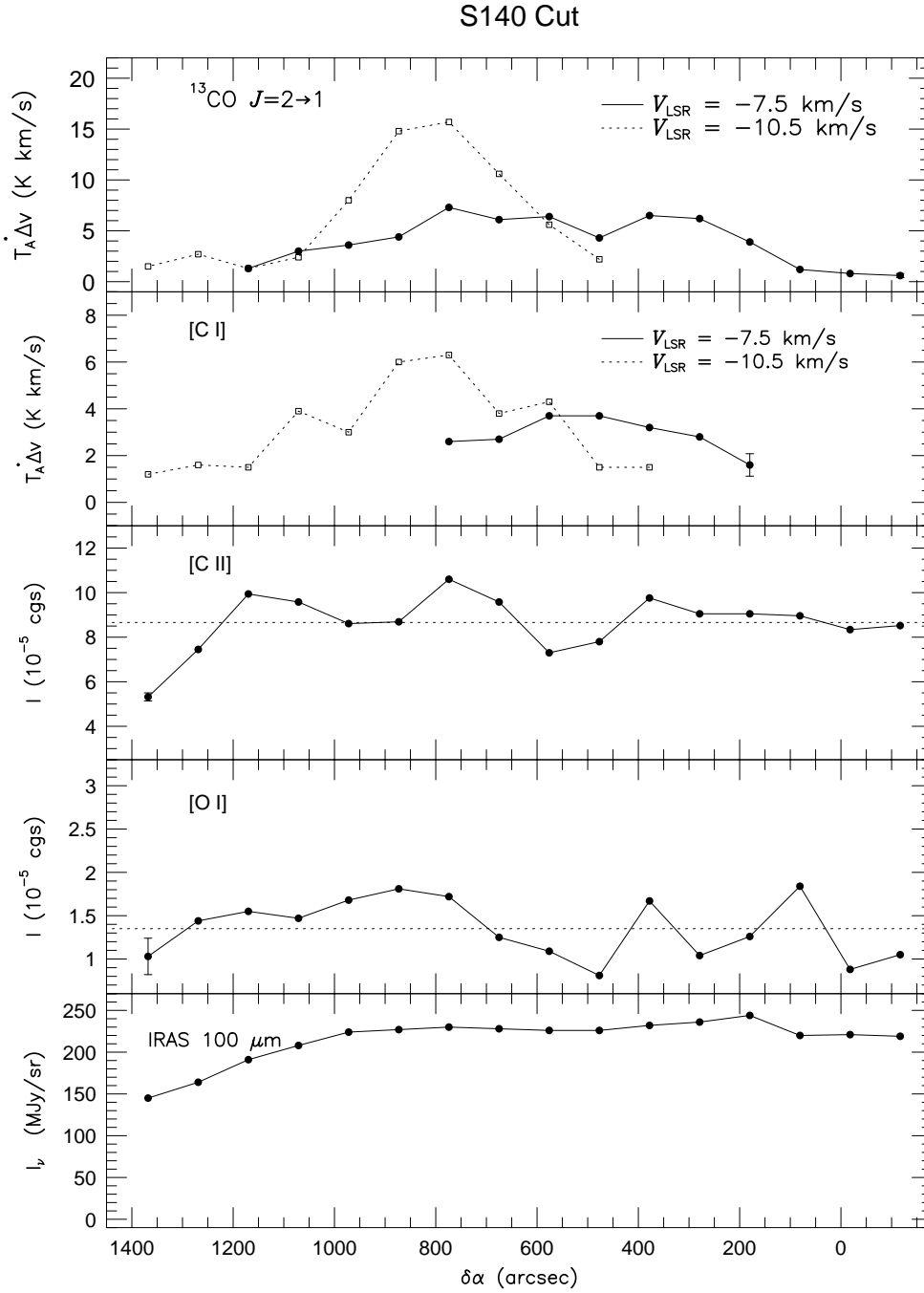


FIG. 4.— Spatial variation along the cut of the $^{13}\text{CO } J=2 \rightarrow 1$, [C I], [C II], [O I] lines and 100 μm continuum. For the $^{13}\text{CO } J=2 \rightarrow 1$ and [C I] lines, both velocity components are shown with different line types. The dotted lines for the panels of the [C II] and [O I] lines are the averaged values of the 16 positions (Avg(16-pos)). Representative error bars are shown on one or the other of the end points; these error bars do not include calibration uncertainties as they do not affect the *shape* of the distribution.

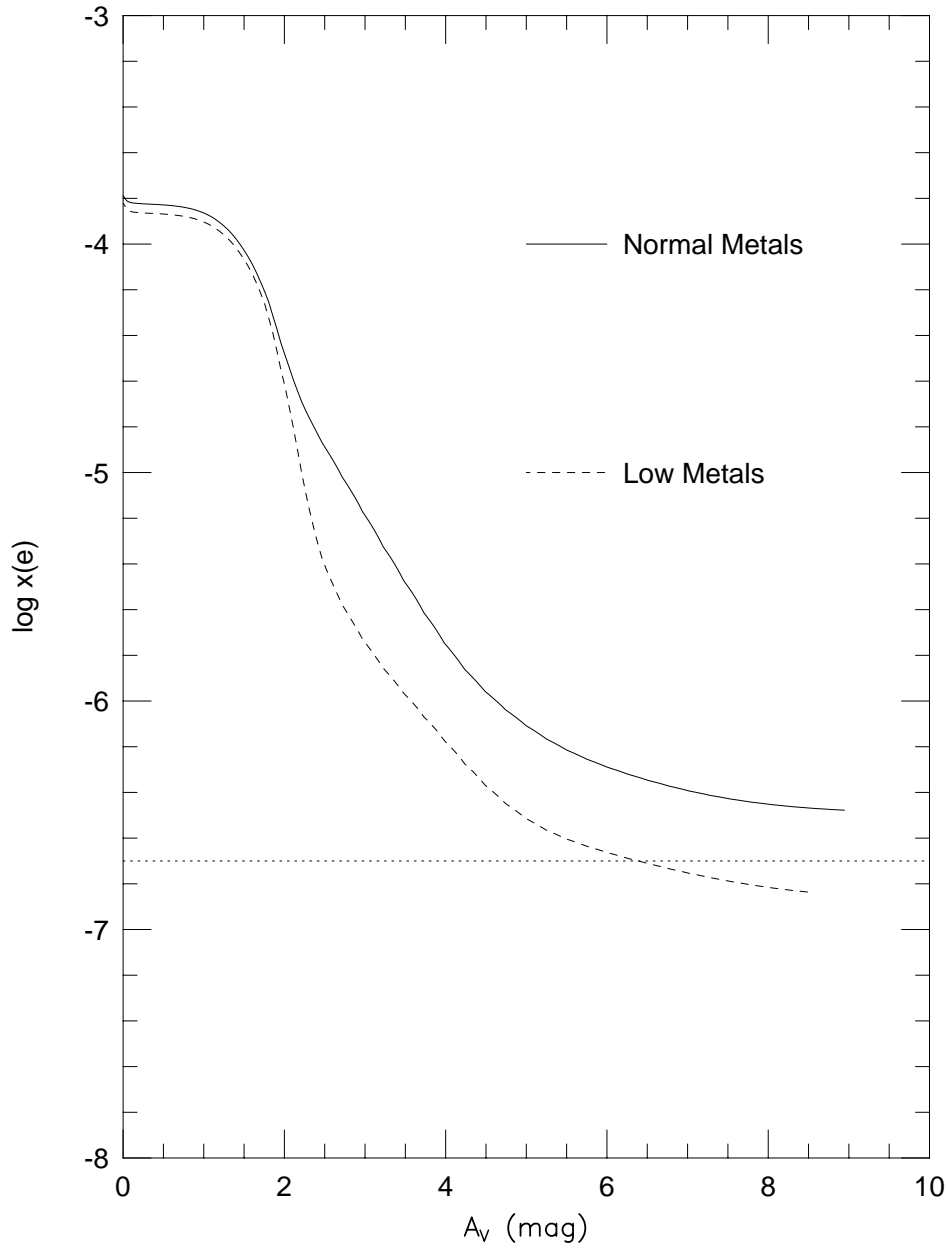


FIG. 5.— Electron abundance versus extinction for two models, both with $G_0 = 17$ and $n = 1000$. The solid line is for normal metals, and the dashed line has low metals. The horizontal dotted line indicates the level of $x(e)$ at which the ambipolar diffusion time equals 30 Myr.

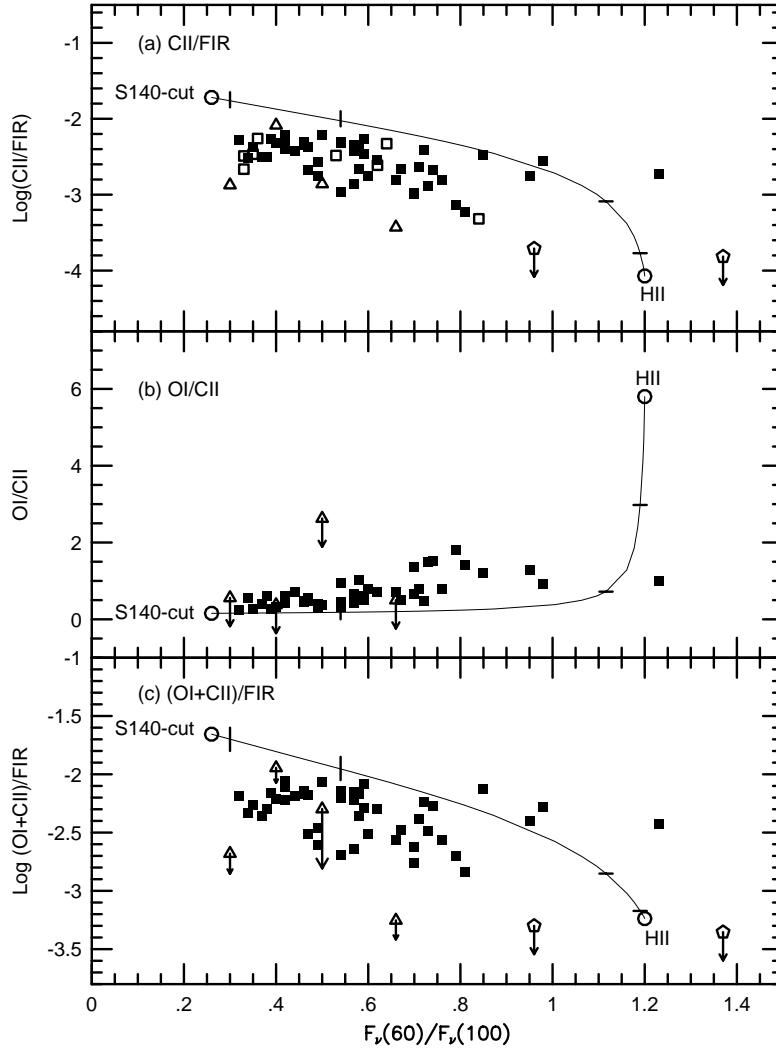


FIG. 6.— Ratios of line and continuum emission from galaxies in the study of Malhotra et al. (2001) compared with the same ratios in Galactic sources. The filled squares show the ratios for galaxies detected in both the $158 \mu\text{m}$ [C II] line and the $63 \mu\text{m}$ [O I] line. Where applicable, the open squares show the ratios for galaxies observed in [C II] but not in [O I]. The open triangles show the locations for galaxies detected in [C II] and observed but not detected in [O I]. In Figure 6c, the detected [C II] emission places a lower bound on the $([\text{O I}] + [\text{C II}])/FIR$ flux ratio. In this panel, the upper limit arrows end at the value corresponding to the measured [C II]/FIR ratio. The open pentagons show the limits on the ratios for galaxies observed but detected in neither [C II] or [O I]. In each panel, the measured ratios for the S140 cut are shown as open circles and labeled. The mixing line connecting these points is based on the fraction of [C II] emission contributed by regions like the S140 cut; the horizontal tickmarks along the curves indicate where such regions contribute 90% and 50% of the [C II] emission to the mixture. The vertical tickmarks show where regions like the S140 cut contribute 90% and 50% of the far-infrared emission.

TABLE 1
THE ISO POSITIONS (1950) OF S140.

Object	S140
Ref. Coord.	(22 ^h 17 ^m 42 ^s , 63°23'15'')
End Position 1	(1368'', 0)
End Position 2	(-1206'', 0)
Step	99''
CSO Off Pos.	(22 ^h 13 ^m 22 ^s , 63°23'15'')
ISO Off Pos.	(22 ^h 05 ^m 46 ^s .7, 63°23'15'')

TABLE 2
LOG OF CSO OBSERVATIONS

Time	Object	Transition	Frequency (GHz)	Δv^a (km s ⁻¹)	Mode ^b	θ_b^c (arcsec)	η_{mb}^d
June 1995	S140	¹² CO $J=2 \rightarrow 1$	230.53797	0.23	RIMG	120	0.80
		¹³ CO $J=2 \rightarrow 1$	220.39870	0.24	RIMG	120	0.80
		C ¹⁸ O $J=2 \rightarrow 1$	219.56032	0.23	RIMG	120	0.80
		¹³ CO $J=3 \rightarrow 2$	330.58800	0.12	RIMG	110	0.80
June 1996	S140	[C I] $J=1 \rightarrow 0$	492.16070	0.08	FD	14	0.45
April 1997	S140	HCO ⁺ $J=3 \rightarrow 2$	267.55762	0.12	RIMG	160	0.80
		HCO ⁺ $J=3 \rightarrow 2$	267.55762	0.12	FD	26	0.70

^aThe velocity resolution of the data.

^bThe setup of the observing mode. RIMG stands for the re-imager mode and FD the full dish.

^cThe beam size.

^dThe main-beam efficiency.

TABLE 3
LINES OBSERVED BY ISO

Line	Wavelength (μm)	E_{up}/k^a (K)	E_{low}/k^b (K)	n_{crit}^c (cm ⁻³)	A (s ⁻¹)	Instr.	Beam ^d
[O I] ³ P ₁ \rightarrow ³ P ₂	63.183705	227.72	0	4.7(5)	8.87(-5)	LWS	1.3×10^{-7}
[C II] ² P _{3/2} \rightarrow ² P _{1/2}	157.7409	91.22	0	2.8(3)	2.4(-6)	LWS	6.65×10^{-8}
H ₂ $J=2 \rightarrow 0$	28.218	509.88	0	5.4(1)	2.9(-11)	SWS	1.3×10^{-8}
H ₂ $J=3 \rightarrow 1$	17.035	1015.12	170.48	1.1(3)	4.8(-10)	SWS	8.9×10^{-9}
H ₂ $J=5 \rightarrow 3$	9.662	2503.82	1015.12	1.9(5)	9.8(-9)	SWS	6.6×10^{-9}

^aThe energy of the upper state of the transition relative the ground state in temperature.

^bThe energy of the lower state of the transition relative the ground state in temperature.

^cThe critical density is A/γ , where γ is the collision rate coefficient.

^dThe LWS beam solid angles are taken from Gry et al. (2001).

TABLE 4
RESULTS OF CSO OBSERVATIONS.

No.	Position	$^{12}\text{CO } 2 \rightarrow 1^{\text{a}}$		$^{13}\text{CO } 2 \rightarrow 1^{\text{b}}$		$^{13}\text{CO } 3 \rightarrow 2^{\text{b}}$		$\text{C}^{18}\text{O } 2 \rightarrow 1^{\text{b}}$		$[\text{C I}]^{\text{b}}$	
		(K)	(K)	(K km s $^{-1}$)	(K km s $^{-1}$)	(K km s $^{-1}$)	(K km s $^{-1}$)	(K km s $^{-1}$)	(K km s $^{-1}$)	(K km s $^{-1}$)	(K km s $^{-1}$)
1	(-117'', 0)	...	1.1	0.6
2	(-18'', 0)	2.7	1.8	0.8
3	(81'', 0)	3.9	3.4	1.2	0.1
4	(180'', 0)	6.7	3.2	3.9	...	1.4	...	0.4	...	1.6	...
5	(279'', 0)	4.5	5.4	6.2	...	1.3	0.5	0.4	...	2.8	...
6	(378'', 0)	4.1	5.8	6.5	...	0.8	...	0.3	...	3.2	1.5
7	(477'', 0)	7.2	5.1	4.3	2.2	1.1	0.9	0.2	0.1	3.7	1.5
8	(576'', 0)	7.2	9.2	6.4	5.6	1.5	1.6	0.3	0.4	3.7	4.3
9	(675'', 0)	7.7	9.5	6.1	10.6	1.4	2.6	0.5	1.4	2.7	3.8
10	(774'', 0)	8.6	11.8	7.3	15.7	2.5	5.7	1.2	2.8	2.6	6.3
11	(873'', 0)	6.5	11.3	4.4	14.8	2.5	6.2	0.4	2.5	...	6.0
12	(972'', 0)	6.3	10.2	3.6	8.0	1.7	0.8	0.1	1.4	...	3.0
13	(1071'', 0)	6.6	7.9	3.0	2.4	0.2	...	3.9
14	(1170'', 0)	5.6	3.6	1.3	1.3	1.5
15	(1269'', 0)	3.7	4.1	...	2.7	1.6
16	(1368'', 0)	3.3	2.4	...	1.5	1.2
“Cloud” ^c		5.6	4.0	4.0	2.0	1.6	0.70	0.39	0.15	2.9	1.9

^aThe peak T_{A}^* of the two velocity components with $V_{\text{LSR}} \sim -7.5 \text{ km s}^{-1}$ and $V_{\text{LSR}} \sim -10.5 \text{ km s}^{-1}$ respectively.

^bThe integrated line intensities of the two velocity components in the region.

^cThe mean integrated line intensities; for the -10.5 km s^{-1} component, the positions with $\delta\alpha$ between 576 and 972 were excluded.

TABLE 5
RESULTS OF THE $\text{HCO}^+ J=3 \rightarrow 2$ LINE OBSERVATIONS.

Position	FWHM Beam	Area ^a		σ (rms)
		(K km s $^{-1}$)	(K)	(K)
(774'', 0)	160	0.09	0.33	0.05
(915'', -71'') ^b	26	...	5.75	0.41
(1170'', 0)	160	0.04
(180'', 0)	160	0.04

^aThe integrated line intensities of the two components are given if applicable, with the first one at $V_{\text{LSR}} \sim -7.5 \text{ km s}^{-1}$ and the second at $V_{\text{LSR}} \sim -10.5 \text{ km s}^{-1}$.

^bPeak position of the $\text{HCO}^+ J=3 \rightarrow 2$ emission when mapped with the full dish. The $\text{HCO}^+ J=3 \rightarrow 2$ emission is clumpy in the area of $300'' \times 300''$ centered at (774'', 0).

TABLE 6
RESULTS OF ISO LWS OBSERVATIONS.

No.	Position	[CII]	[OI]	Ratio	IRAS(60 μm) ^a	IRAS(100 μm) ^a
	(arcsec)	(10^{-5} erg cm^{-2} s^{-1} sr^{-1})	[OI]/[CII]		(MJy sr^{-1})	
1	(-117,0)	8.52±0.18	1.05±0.06	0.12	57.3	219
2	(-18,0)	8.34±0.18	0.88±0.19	0.11	57.2	221
3	(81,0)	8.96±0.18	1.84±0.12	0.21	58.8	220
4	(180,0)	9.05±0.27	1.26±0.19	0.14	66.1	244
5	(279,0)	9.05±0.27	1.04±0.17	0.12	61.5	236
6	(378,0)	9.76±0.53	1.67±0.25	0.17	56.2	232
7	(477,0)	7.80±0.35	0.81±0.18	0.10	52.9	226
8	(576,0)	7.30±0.27	1.09±0.21	0.15	52.5	226
9	(675,0)	9.58±0.27	1.25±0.19	0.13	54.3	228
10	(774,0)	10.6±0.53	1.72±0.19	0.16	58.8	230
11	(873,0)	8.69±0.18	1.81±0.23	0.21	63.4	227
12	(972,0)	8.61±0.36	1.68±0.32	0.20	63.0	224
13	(1071,0)	9.58±0.44	1.47±0.23	0.15	58.3	208
14	(1170,0)	9.94±0.18	1.55±0.11	0.16	51.3	191
15	(1269,0)	7.45±0.18	1.44±0.19	0.19	44.8	164
16	(1368,0)	5.32±0.18	1.03±0.21	0.19	39.6	145
	Avg(16-pos) ^b	8.66±1.27	1.35±0.34	0.16±0.04		
	ISO-OFF	1.69±0.18	0.46±0.20	0.27	9.6	47.7
	IRS1 ^c	44±2	68±3	1.55 ± 0.10		

^aThe IRAS fluxes at 60 μm and 100 μm at the S140 cut positions and the S140 ISO off position.

^bThe average line fluxes and ratios of all 16 positions. The errors are the standard deviation of the values at the 16 positions.

^cThe average of the 4 existing measurements toward this position. The error reflects the standard deviation of the individual measurements.

TABLE 7
RESULTS OF ISO SWS OBSERVATIONS.

No.	Position	H ₂ $J = 2 \rightarrow 0$	H ₂ $J = 3 \rightarrow 1$	H ₂ $J = 5 \rightarrow 3$	T_{32} ^a	T_{53} ^a
	(arcsec)	(10 ⁻⁵ erg cm^{-2} s^{-1} sr^{-1})			(K)	(K)
1	(-117,0)	1.0±0.5	1.1±0.6	< 0.6	109 ± 30	< 320
"F"	(743,0)	0.8±0.4	0.8±0.3	< 0.6	106 ± 25	< 320
14	(1170,0)	1.3±0.4	0.9±0.4	0.8 ± 0.3	98 ± 18	350 ± 50

^aThe excitation temperature between upper J levels that yields the observed line ratio, assuming that the ortho-para ratio is in LTE.